Quench-Spot Detection for Superconducting Accelerator Cavities Via Flow Visualization in Superfluid Helium-4

Shiran Bao[1,2] and Wei Guo[1,2,*]

[1]*National High Magnetic Field Laboratory, 1800 East Paul Dirac Drive, Tallahassee, Florida 32310, USA*
[2]*Mechanical Engineering Department, Florida State University, Tallahassee, Florida 32310, USA*

Superconducting radio-frequency (SRF) cavities, cooled by superfluid helium-4 (He II), are key components in modern particle accelerators. Quenches in SRF cavities caused by Joule heating from local surface defects can severely limit the maximum achievable accelerating field. Existing methods for quench-spot detection include temperature mapping and second-sound triangulation. These methods are useful but also have known limitations. Here we describe an alternative method for surface quench-spot detection by visualizing the heat transfer in He II via tracking He_2^* molecular tracer lines. A proof-of-concept experiment is conducted, in which a miniature heater mounted on a plate is pulsed on to simulate a surface quench spot. A He_2^* tracer line created nearby the heater deforms due to the counterflow heat transfer in He II. By analyzing the tracer-line deformation, we well reproduce the heater location within a few hundred microns, which clearly demonstrates the feasibility of this alternative technology. Our analysis also reveals that the heat content transported in He II is only a small fraction of the total input heat energy. We show that the remaining energy is essentially consumed in the formation of a cavitation zone near the heater. By estimating the size of this cavitation zone, we discuss how the existence of the cavitation zone may explain a decades-long puzzle observed in many past second-sound triangulation experiments.

I. INTRODUCTION

Superconducting radio-frequency (SRF) cavities are key components in many modern particle accelerators due to their high-Q-factors [1]. When these cavities are cooled by superfluid helium-4 (He II) to around 2 K, electric power injected in the cavities can generate extremely high electric field that allows charged particles to be accelerated to high energies over short distances. The maximum accelerating gradient of typical SRF cavities is in the range of 25–30 MW/m with a record value of 45 MW/m [2]. This maximum gradient is limited by the breakdown of the superconductivity of the cavities, a phenomenon known as "quench." Quenches can be caused by Joule heating from tiny (i.e., about 1–10^2 μm in radius) resistive surface defects on the cavity inner walls (such as impurities, pits, cracks, scratches) or local phase transition caused by trapped magnetic fluxes [3]. When the temperature at the edge of the resistive region exceeds the superconducting phase-transition temperature, the surrounding region also becomes normal conducting. This process then spreads out rapidly over the entire cavity, causing the stored energy to convert to heat around the defect area within a few milliseconds [3].

The maximum accelerating gradient of SRF cavities can be improved by removing the surface defects via mechanical grinding, tumbling the cavity, and electron or laser remelting [4–6]. In order to locate the surface defects, a multichannel temperature mapping (T-mapping) method was first developed in Refs. [7,8]. This method requires a large number of temperature sensors (i.e., over 1000) in good thermal contact with the outer surface of the cavity and is often applied at a cavity accelerating gradient just below the quench threshold. The continuous Joule heating from a surface defect raises the local temperature, which manifests the defect location in the temperature map. Despite the usefulness of T mapping, the spatial resolution is limited by the spacing between sensors (i.e., of order 1 cm). Furthermore, the installation of a large amount of sensors makes the application of this method an extremely laborious task [6]. An alternative way to apply T mapping is to scan the cavity surface using a rotating arm with just a few sensors arranged in a stripe. Nevertheless, to allow smooth rotation, a gap between the sensors and the cavity surface is required, which limits the detection sensitivity [9,10].

A more convenient noncontacting quench-spot detection method based on second-sound triangulation was later introduced by a team at Cornell University [11]. This method makes use of the unique properties of He II. In

---

*wguo@magnet.fsu.edu

the superfluid phase below $T_\lambda \simeq 2.17$ K, He II can be regarded as a mixture of two interpenetrating fluids: a viscous normal fluid that carries all the entropy and an inviscid superfluid that possesses zero entropy [12]. This two-fluid system can support two distinct sound modes: the first sound, i.e., an ordinary pressure-density wave in which both fluids move in phase, and the second sound, i.e., a temperature-entropy wave in which the two fluids move out of phase [13]. When the cavity quenches, the heat generated in the defect region is conducted promptly to the cavity outer surface. This heat is then released into He II, causing the generation and propagation of second-sound waves, in which a counterflow of the two fluids can establish [14]. These second-sound waves can be detected using sensors such as oscillating superleak transducers (OST) [11,15], resistive temperature detectors (RTD) [16], and transition edge sensors (TES) [17]. By measuring the time-of-arrival of the second-sound waves at three or more such sensors and implementing triangulation, the surface defect can, in principle, be located. However, a mystery was observed in many second-sound triangulation experiments. In order for the triangulation to converge to the cavity surface, a second-sound speed faster than standard literature values must be assumed [11,18–23]. This calculated location can have an uncertainty of 5–10 mm from the actual defect location [24], making it difficult for subsequent inspection of the submillimeter defect [25,26]. Various models have been proposed to explain the puzzling fast second sound, such as spreading of the heat in the cavity walls [19,21,27], possible delay in detecting the start of the quench [19,20], and nonlinear effect that affects the second-sound shock speed at high heat fluxes [22,28]. However, none of these models can offer a convincing explanation that systematically accounts for various observations [6,22,23].

In this paper, we discuss an alternative noncontacting method for quench-spot detection by visualizing quench-induced thermal counterflow in He II using a He$_2^*$ molecular tracer-line tagging technique developed in our laboratory [29–31]. A proof-of-concept experiment is conducted, in which a miniature heater mounted on a plate in He II is utilized to simulate a surface quench spot. A He$_2^*$ tracer line created nearby the heater deforms as a result of the transient counterflow. The experimental techniques are discussed in detail in Sec. II. In Sec. III, we present the analysis results. We show that by analyzing the tracer-line deformation, the heater location can be determined with an uncertainty of only a few hundred microns. Our analysis also reveals that the heat transported through He II is just a small fraction of the total input heat energy. We show, in Sec. IV, that the remaining energy is largely consumed in the formation of a cavitation zone near the heater. The creation and collapsing of vapor bubbles inside the cavitation zone can convert the heat energy to acoustic energy. By estimating the size of the cavitation zone, we

propose a model that explains the puzzling faster second sound and gives estimated excess second-sound velocities in quantitative agreement with the observations in triangulation experiments. We also discuss how our visualization technique may be advanced for practical SRF cavity quench-spot detection. A brief summary is given in Sec. V.

II. EXPERIMENTAL TECHNIQUES

The optical cryostat used in our proof-of-concept experiment is shown schematically in Fig. 1. An aluminum cubic helium cell with an inner side length of 3 inches is connected to a pumped helium bath whose temperature is maintained at 1.85 K, typical of the operation temperature of SRF cavities, by regulating the vapor pressure in the bath. To examine the relevant heat-transfer processes in a real quench event, we note that the energy stored in a SRF cavity (i.e., of order 1–10 J) is converted to heat in a few milliseconds [3]. As the heat is conducted to the cavity outer surface, the heated region can expand to an area of order 1–10 cm^2 with the hottest spot at the area center. Therefore, the instantaneous heat flux into He II is of order 10^2–10^3 W/cm^2 [22]. In order to simulate this heat flux in our experiment, we utilize an array of 5×5 miniature thick-film resistors (surface area $A_h = 0.8 \times 0.8$ mm^2) installed on an insulated printed circuit board (PCB). The resistance of these resistor heaters is measured to be 49.7 ± 0.3 Ω at 1.85 K. A rectangular voltage pulse with a duration of 1–4 ms and an adjustable amplitude up to 10 V can be applied to a selected heater, giving rise to a heat flux into He II up to 315 W/cm^2 at the heater surface. The size of our heaters is relatively small compared to the size of the heated area on the cavity outer surface. Nevertheless, this heater size is common among quench-spot testing experiments and simulations
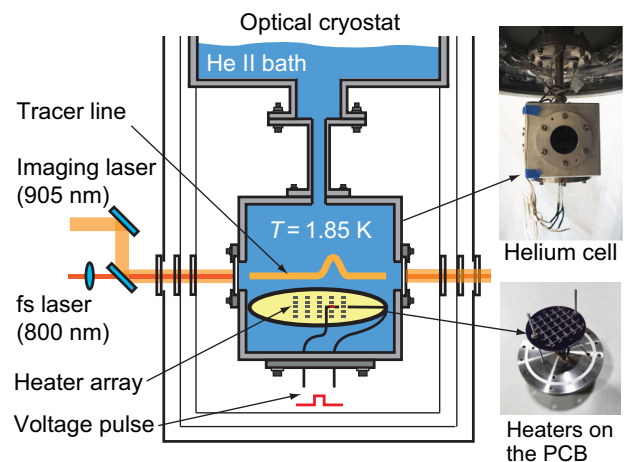

FIG. 1. Schematic of the experimental setup (not to scale).

[22,32–34] and is also desired for testing the resolution of our flow-visualization-based detection method.

The heat ejected into He II leads to the generation of a second-sound shock wave followed by a thermal counter-flow of the two fluids (see detailed discussions in Sec. III). In order to visualize the flow of the normal fluid that carries the heat content in He II, we adopted our He_2^* molecular tracer-line tagging technique [30]. A 35-fs pulsed laser beam at 800 nm with a repetition rate of 5 kHz and a pulse energy of about 60 μJ is focused to pass through the helium cell. Due to the strong instantaneous laser field, some helium atoms are ionized along the fs-laser beam path in the focal region. The recombination of the electrons and helium ions then leads to the formation of metastable He_2^* triplet molecules [35]. These molecules form tiny bubbles in He II (i.e., 6 Å in radius [36]) and have a lifetime of about 13 s [37]. Above 1 K, they are completely entrained by the viscous normal fluid since Stokes drag easily dominates other forces for small molecules. This line of He_2^* molecular tracers can then be driven to produce 640-nm fluorescent light by a 5-ns pulsed imaging laser at 905 nm [38]. The imaging laser in our experiment has a repetition rate of 500 Hz and is shaped into a laser sheet (thickness, 1 mm; height, 5 mm) that covers the entire region traversed by the tracer lines. The fluorescence is captured by an intensified CCD (ICCD) camera mounted perpendicular to the tracer-line plane. Typically, five–six imaging pulses are used to produce good-quality images. This flow-visualization technique is successfully utilized in our quantitative studies of quantum turbulence in He II [31,39–43].

By adjusting the position of the fs-laser beam, we can create a He_2^* tracer line nearly in parallel to the PCB at a height h right above a chosen heater. Without turning on the heater, an image of the tracer line can be taken as a reference (i.e., the baseline). A typical baseline image is shown in Fig. 2(a). The thickness of the baseline is about 100 μm, which matches the thickness of the fs-laser beam in the focal region. The time delay between the creation and imaging of the baseline (i.e., the drift time t_d) is set to zero. Indeed, when there is no flow in He II, the baseline remains straight at its original position regardless of the duration of the drift time. In the tests for locating the heater, we first create a tracer line and then turn on the heater by applying a voltage pulse of duration Δt. The instantaneous heating power $\dot{Q}_0$ (and hence the heat flux $q_0 = \dot{Q}_0/A_h$) can be controlled by varying the voltage on the heater. An initially straight tracer line deforms due to the normal-fluid flow accompanying the heat transfer. After a typical drift time t_d of 20–30 ms, we send in the imaging pulses to visualize the deformed line. Figure 2(b) shows an example image of the deformed tracer line following a heat pulse of $q_0 = 287$ W/cm^2 and $\Delta t = 2$ ms. As we discuss in Sec. IV, in our experiment the heat is transported in He II essentially by second-sound waves, which propagates at a speed $c_2 = 19.5$ m/s at 1.85 K [44]. It takes less than 1 ms for
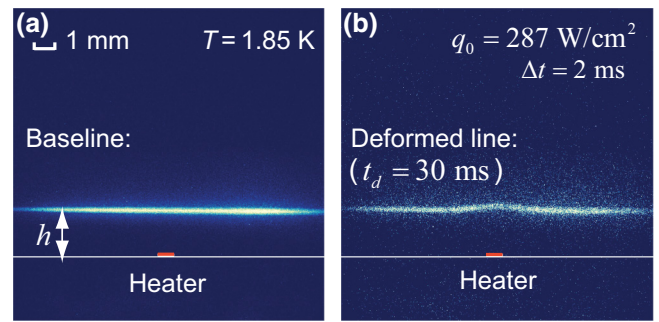

FIG. 2. Typical images showing (a) a baseline created at $h = 2.13$ mm above the heater, and (b) a deformed tracer line following a heat pulse of $q_0 = 287$ W/cm^2 and $\Delta t = 2$ ms.

the second-sound waves to pass across the entire tracer line. Indeed, when t_d is greater than 2–3 ms, the tracer-line deformation is observed to be independent of t_d.

III. ANALYSIS AND RESULTS

Apparently, the deformation of the tracer lines contains important information about the heater location and the heat content transported through He II. In order to extract this information, a detailed understanding of the relevant heat-transfer processes in He II and the expected motion of the tracer lines is needed.

A. Transient heat transfer in He II

It is known that heat transfer in He II is via a counter-flow of the two fluid components, i.e., the normal fluid flowing away from the heat source carrying all the heat content, while the superfluid moves in the opposite direction to compensate the fluid mass [14]. The heat flux q is related to the normal-fluid velocity v_n as $q = \rho s T v_n$, where ρ and s are the helium density and specific entropy, respectively. When the heat flux is above a threshold of order 10^{-2} W/cm^2 [45], quantized vortex lines are produced in the superfluid [46], each carrying a single quantum of circulation $\kappa \approx 9.97 \times 10^{-4}$ cm^2/s around its angstrom-sized core [47]. A mutual friction between the two fluids arises due to scattering of the thermal excitations off the vortices [46]. For a transient heat transfer from a point heat source in He II (see the schematics in Fig. 3), the heat content is transported by a second-sound zone propagating at the speed c_2 [14]. The thickness of the second-sound zone is about $c_2 \Delta t$, within which a counterflow can establish.

It is worthwhile noting that Shimazaki et al. observed that in one-dimensional (1D) transient heat transfer of He II through a circular pipe, the injected heat is carried uniformly in the second-sound zone at low heat fluxes [48]. As the heat flux increases, the vortex-line density L (i.e., vortex-line length per unit volume) increases. Above a threshold heat flux (i.e., about 5 W/cm^2 for Δt of a few milliseconds), the interaction between the second-sound
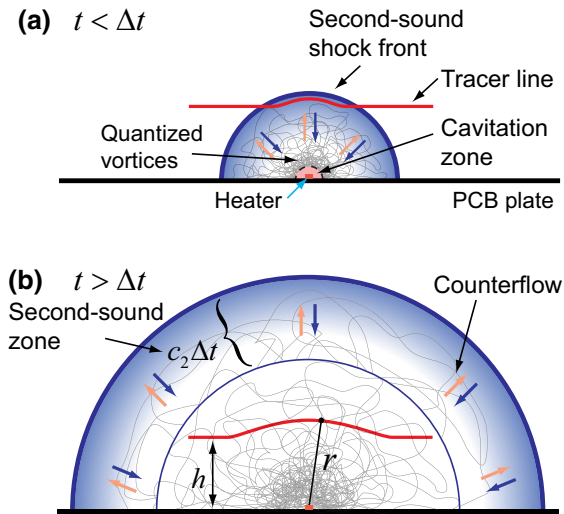
FIG. 3. Schematics showing the transient heat transfer processes from a point heat source in He II. (a) At time t less than the heat pulse duration Δt, a cavitation zone forms near the heater. (b) At $t > \Delta t$, some heat is carried out by the propagating second-sound zone.

waves and the dense vortices can strongly distort the temperature profile in the second-sound zone, leading to the so-called "limiting profile" with the formation of a second-sound shock front [48,49]. In this situation, a significant fraction of the heat is converted to vortex energy, which releases diffusively as the tangle decays. Nevertheless, as we show in Sec. IV, the heat energy that goes to the vortices in our experiment is *negligible*. This is because, unlike in the 1D heat transfer case, the heat flux drops rapidly away from a point heat source, and so does the vortex-line density.

Another process that is relevant to transient heat transfer in He II is film boiling at high heat fluxes [14]. The threshold heat flux for film boiling to occur in saturated He II depends on the duration of the applied heat pulse. For a heat pulse of a few milliseconds, this threshold is about 15 W/cm^2 [48–50]. In our experiment, the instantaneous heat flux from the heater surface is much higher than the film boiling threshold. Therefore, at $t < \Delta t$, a cavitation zone must form in the vicinity of the heater, as depicted in Fig. 3(a). Outside this cavitation zone, some heat energy can be carried out by the propagating second-sound zone.

B. Deformation of He$_2^*$ tracer lines

To evaluate the deformation of a He$_2^*$ tracer line, let us consider a line segment at an initial distance r_0 from the miniature heater. As the second-sound shock front arrives at this line segment, it starts to move at the local normal-fluid velocity v_n. If we assume that the heat transfer is isotropic towards all directions from the heater, v_n is always along the radial direction and therefore the radial

displacement of the line segment dr in time dt is given by

$$dr = v_n \times dt = \frac{q(r)}{\rho s T} \times dt, \qquad (1)$$

where $q(r) = \dot{Q}_s/(2\pi r^2)$ is the heat flux across the hemisphere of radius r, with $\dot{Q}_s$ being the instantaneous rate of heat transfer over the entire hemispherical surface. By integrating Eq. (1), one can derive the final distance r_f of the line segment from the heater as

$$r_f^3 = r_0^3 + \frac{3}{2\pi\rho s T}\int_{t_0}^{t_0+\Delta t} \dot{Q}_s dt = r_0^3 + \frac{3Q_s}{2\pi\rho s T}, \qquad (2)$$

where t_0 is the time that the second-sound zone first arrived at the line segment, and Q_s denotes the total heat energy carried by the second-sound zone.

The assumption that the heat transfer is isotropic towards all directions holds true only if the heater size is small (i.e., approximately a point heat source) and that the effect of the PCB can be ignored. Note that due to the no-slip boundary condition of the normal fluid on the PCB, the heat flux within a boundary layer from the PCB surface must be different from that in bulk He II. The thickness of this boundary layer increases along the radius of the PCB and can be estimated to be about 300 μm near the edge of the PCB [51]. Therefore, any relevant effect can be safely neglected.

Based on Eq. (2), the profile of a deformed tracer line can be computed from a given initial baseline, if we know the position x_0 of the heater on the PCB and the total heat Q_s carried by the second-sound zone. In our analysis, we first adopt an algorithm developed by Pulkkinen *et al.* [52] to extract the locations of the baseline and the deformed line from the fluorescence images. We then set x_0 and Q_s as two adjustable parameters to evolve the baseline profile so that a least-squares fitting to the deformed line profile can be made. Typical examples of curve fittings to the deformed tracer lines based on their corresponding baselines are shown in Fig. 4. One can see that this simple model very well reproduces the deformed line profiles. Figure 4 also shows that the deformation of the tracer line becomes weaker when it is created at a larger distance h from the heater. The minimum line deformation that can be resolved is comparable to about half the thickness of the tracer line. For a heat pulse of $q_0 = 287$ W/cm^2 and $\Delta t = 2$ ms, we estimate that the maximum distance of the tracer line from the heater can reach $h_{\max} \simeq 5$ mm. Nevertheless, we note that based on Eq. (2), the displacement of the tracer line depends on the total heat transported through He II instead of the instantaneous heat flux on the heater surface. In a real quench event, the heat deposited in He II is comparable to the total energy stored in the cavity (i.e., of order 1–10 J [3]), which is 2 to 3 orders of magnitude larger than the heat produced by our miniature heater
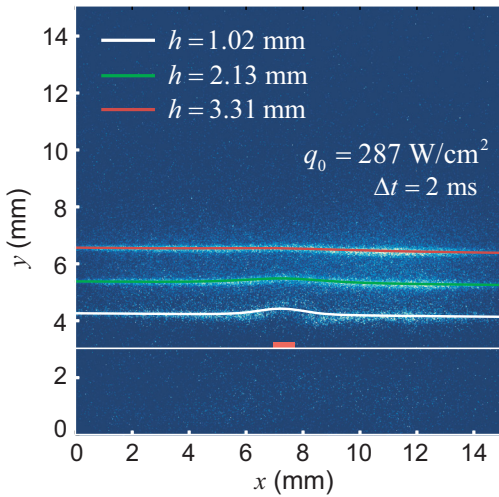
FIG. 4. Examples of curve fittings to deformed tracer lines created at different initial height h above the heater.

(i.e., of order 10 mJ). Therefore, we would expect resolvable line deformation even for tracer lines created at *a few centimeters* away from a real cavity surface.

C. Analysis results

We have conducted the heater detection tests at various heat fluxes $q_0 = \dot{Q}_0/A_h$ and pulse durations Δt. The values of x_0 and Q_s can be determined through the curve fittings as we previously discussed. The results are collected in Table I. Figure 5 shows typical derived heater location x_0

in comparison with the actual center position of the heater (i.e., $x_h = 7.46$ mm). For each test, we normally repeat our measurement ten times so that the result uncertainty can be estimated. The fact that the obtained x_0 is always within a few hundred microns from the actual heater location, regardless of the applied heat flux q_0 and the pulse duration Δt, clearly proves the feasibility of this visualization-based noncontacting quench-spot-detection technology.

In Fig. 6, we show the ratio of the heat energy Q_s carried by the second-sound zone to the total heat generated by the heater $Q_0 = \dot{Q}_0 \Delta t$ as a function of q_0 and Δt. This ratio Q_s/Q_0 appears to be weakly dependent on q_0 and nearly independent of Δt. The knowledge about the exact values of Q_s, which is not available from typical second-sound triangulation measurements, provides us a clue about the origin of the "fast" second sound evinced in those triangulation experiments (see detailed discussions in Sec. IV). From Table I, we also note that under the same heater conditions, the fit values for Q_s at $h = 1.02$ mm appear to be much smaller than those obtained at larger h. This is likely due to the fact that the miniature heater can no longer be treated as a point heat source when the tracer line is placed too close.

IV. DISCUSSIONS

A. Partition of the heat energy

Since the heat Q_s transported through He II by the second-sound zone is only a fraction of the total heat Q_0 generated by the heater, a natural question one may raise is

TABLE I. Results of the curve fittings at various experimental conditions.

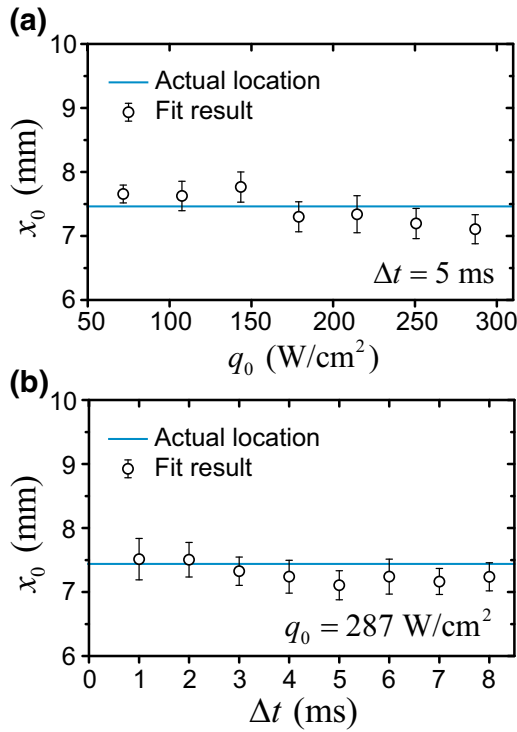| h (mm)	q_0 (W/cm^2)	Δt (ms)	t_d (ms)	x_0 (mm)	Q_s (mJ)	Q_s/Q_0	r_c (mm)
1.02	144	2	20	7.64 ± 0.42	0.17 ± 0.10	9.05%	0.30
1.02	215	2	20	7.30 ± 0.18	0.24 ± 0.06	8.35%	0.35
1.02	287	2	20	7.25 ± 0.13	0.29 ± 0.15	8.02%	0.39
1.98	78	5	20	7.66 ± 0.14	0.68 ± 0.11	29.43%	0.38
1.98	108	5	20	7.63 ± 0.23	1.12 ± 0.24	32.50%	0.49
1.98	144	5	20	7.77 ± 0.24	1.20 ± 0.18	26.07%	0.50
1.98	179	5	20	7.30 ± 0.23	1.70 ± 0.31	29.70%	0.60
1.98	215	5	20	7.34 ± 0.29	1.43 ± 0.19	20.85%	0.55
1.98	251	5	20	7.20 ± 0.24	1.78 ± 0.33	22.18%	0.61
1.98	287	1	20	7.51 ± 0.32	0.36 ± 0.15	19.52%	0.62
1.98	287	2	20	7.50 ± 0.27	0.75 ± 0.21	20.35%	0.63
1.98	287	3	20	7.33 ± 0.22	1.17 ± 0.30	21.25%	0.64
1.98	287	4	20	7.24 ± 0.26	1.73 ± 0.24	23.58%	0.68
1.98	287	5	20	7.11 ± 0.23	1.76 ± 0.20	19.20%	0.61
1.98	287	6	20	7.24 ± 0.27	1.96 ± 0.19	17.82%	0.59
1.98	287	7	20	7.16 ± 0.20	2.48 ± 0.34	19.27%	0.61
1.98	287	8	20	7.24 ± 0.22	2.40 ± 0.39	16.31%	0.56
2.13	287	2	20	7.46 ± 0.38	0.89 ± 0.21	24.42%	0.69
2.13	287	2	30	7.52 ± 0.18	0.98 ± 0.33	26.92%	0.72
2.13	287	2	40	7.38 ± 0.10	0.93 ± 0.30	25.59%	0.70
3.31	287	2	20	7.05 ± 0.41	0.85 ± 0.19	23.30%	0.67

FIG. 5. Fitting results of the heater location x_0 versus (a) heat flux q_0 at a fixed pulse duration, and (b) pulse duration Δt at a fixed heat flux. $h = 1.98$ mm for these measurements.

as follows: where does the remaining energy go? Indeed, a similar phenomenon was observed in earlier experiments on 1D transient heat transfer of He II through uniform pipes [48,50,53]. It is observed that the heat carried by the second-sound zone dropped significantly at heat fluxes greater than about 5 W/cm². This observation is interpreted as due to the energy consumed in the formation of a dense vortex tangle and the film boiling in front of the heater.

The time evolution of the vortex-line density L in a counterflow is governed by Vinen's equation [46]:

$$\frac{dL}{dt} = \alpha v_{ns}L^{3/2} - \beta \kappa L^2, \tag{3}$$

where $v_{ns}=(\rho/\rho_s)v_n=q/\rho_s sT$ is the relative velocity of the two fluids, and α and β are dimensionless parameters with known values [44]. In a steady-state heat transfer, the equilibrium vortex density is given by $L_0 = (\alpha/\beta\kappa)^2 v_{ns}^2$. The time τ taken for the line density to grow to the equilibrium value depends on the heat flux q as $\tau = aq^{-n}$, with a and n being temperature-dependent constants [54,55]. For a heat flux of order 10 W/cm², $\tau \simeq 0.3$ ms. Therefore, in transient heat transfer at high heat fluxes with a duration longer than 1 ms, it is reasonable to assume the equilibrium line density L_0 in relevant analysis. The energy E associated with a random tangle of vortices per unit mass of He II is

given by [56]

$$E \approx \frac{\rho_s \kappa^2}{4\pi\rho}L\ln\left(\frac{l}{\xi_0}\right), \tag{4}$$

where $l = L^{-1/2}$ is the mean vortex-line spacing and $\xi_0 \simeq 1$Å is the healing length for He II. Combining Eqs. (3) and (4), one can derive an equation for the change in rate of the vortex energy $\dot{E} = \dot{E}_g - \dot{E}_d$, where the generation term $\dot{E}_g$ takes the following form:

$$\dot{E}_g = \alpha v_{ns}L^{3/2}\frac{\rho_s \kappa^2}{4\pi\rho}\left[\ln\left(\frac{l}{\xi_0}\right) - 0.5\right]. \tag{5}$$

This generation term essentially accounts for the rate of energy that goes from the second-sound zone to the formation of vortices per unit mass of He II. Therefore, the heat flux $q(r)$ in the second-sound zone must satisfy

$$\frac{d\left[q(r)A\right]}{dr} = -\dot{E}_g A/\rho, \tag{6}$$

where A is the cross-section area at r, i.e., $2\pi r^2$ in our experiment or a constant in those 1D tube heat-transfer experiments. Equation (6) allows one to evaluate the heat-transfer rate $\dot{Q} = q(r)A$ associated with the propagating second-sound front at a distance r from the heat source.
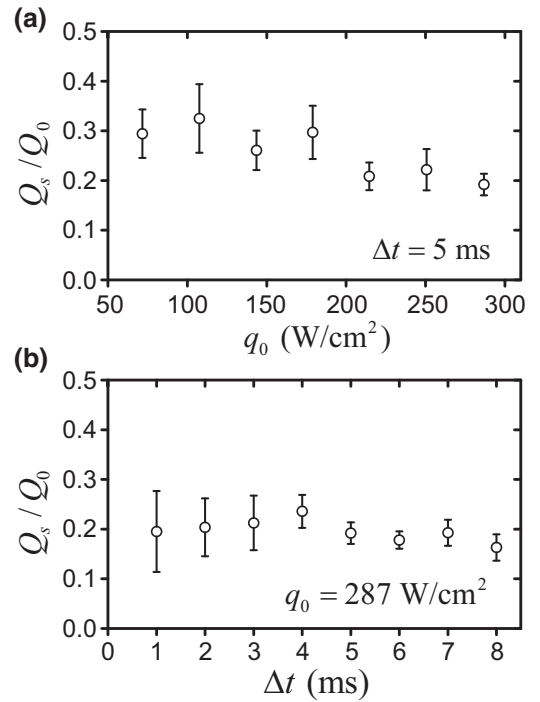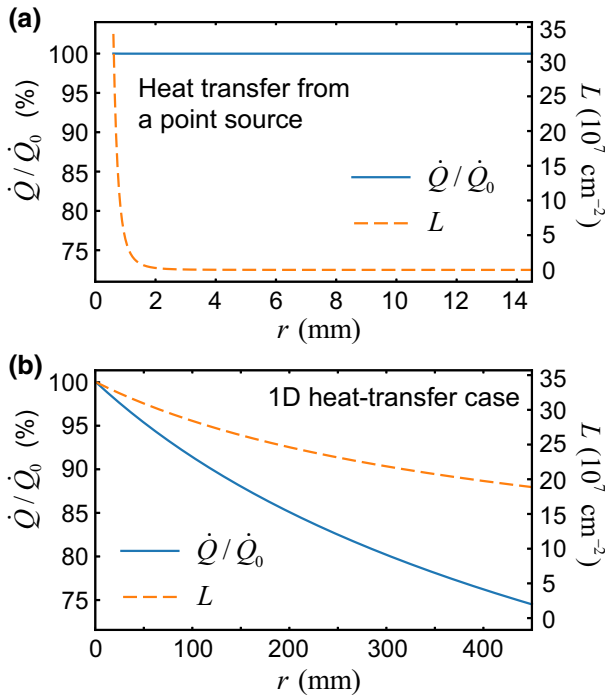

FIG. 6. The ratio of the heat energy Q_s carried by the second-sound zone to the total heat generated by the heater $Q_0 = \dot{Q}_0\Delta t$ as a function of (a) heat flux q_0 and (b) pulse duration Δt. $h = 1.98$ mm for these measurements.

FIG. 7. Vortex-line density L and heat transfer rate $\dot{Q} = q(r)A$ associated with the propagating second-sound front at a distance r from (a) a hemispherical surface with a radius of $r_c = 0.6$ mm and a surface heat flux of $q_c = 15$ W/cm^2; and (b) a planar heater in a pipe that supplies the same heating power, i.e., $\dot{Q}_0 = q_c \times 2\pi r_c^2$.

The calculation results for both our experiment and the 1D heat-transfer case are shown Fig. 7. It is clear that in our experiment, L drops rapidly with r since the heat flux q decreases nearly as $1/r^2$. Significant temperature gradient exists only within a thin thermal layer where L is high. The heat energy carried by the second-sound zone suffers no noticeable attenuation. On the other hand, in the 1D heat-transfer case, the vortex density remains high even at tens of centimeters away from the planar heater. The heat energy carried by the second-sound zone is constantly converted to vortex energy. This vortex energy then decays into heat that slowly diffuses out [14], which causes a broad temperature rise following the second-sound zone, as observed in some 1D heat-transfer experiments [48].

Accepting the conclusion that the vortex effect is negligible in our experiment, the only other mechanism that can consume the heat energy is the formation of the cavitation zone. The heat energy deposited near the heater surface can vaporize the helium atoms and lead to the nucleation and growth of small vapor bubbles. In those 1D heat-transfer experiments [48], it is suggested that the fraction of the heat energy consumed by this process increases with increasing the heat flux q_0 from the heater surface and can reach about 50% at $q_0 = 40$ W/cm^2. Considering the much higher heat fluxes from the miniature heater surface

in our experiment, it is not surprising to see that over 70% of the heat energy goes to the vapor bubbles.

We may make an order of magnitude estimation of the growth rate of the vapor bubbles. Considering a hemispherical vapor bubble that sits on the surface of the heater, if we assume that the injected heat is all utilized to vaporize the helium atoms, the growth of the bubble radius R is then governed by [57]

$$L_v \rho_v \frac{d}{dt}\left(\frac{2\pi}{3}R^3\right) = \pi R^2 q_0, \qquad (7)$$

where L_v and ρ_v are the helium latent heat and the vapor density in the bubble, respectively. According to Eq. (7), $\dot{R} = q_0/2L_v\rho_v$. For the heat flux used in our experiment or in typical cavity quenching (i.e., 10^2–10^3 W/cm^2), the bubble surface velocity $\dot{R}$ can exceed the first-sound speed in He II (i.e., $c_1 = 230$ m/s at 1.85 K [44]), which leads to the emission of strong first-sound shock waves due to the finite compressibility of He II. As a vapor bubble grows, the combined effects of buoyancy, shear lift, and contact pressure force may detach the bubble from the heater surface [58]. Without the heat input, the bubble starts to shrink. Due to the existence of the heater surface nearby, the bubble collapses asymmetrically, leading to the formation of a micro-jet that can penetrate the bubble and impinge on the heater surface [59–61]. This process can again lead to strong first-sound emission. Therefore, the heat energy consumed by the vapor bubbles in the cavitation zone can essentially convert to acoustic energy carried by the first sound. Indeed, sound bursts and associated pressure spikes accompanying film boiling in He II have been observed experimentally [62,63]. Since the first-sound waves only cause the fluid parcels in He II to oscillate around their equilibrium positions, there is barely any detectable effect using either our flow-visualization technique or those second-sound sensors.

B. Origin of the "fast" second sound

The conclusion that a large fraction of the heat energy is utilized in the creation of the cavitation zone motivates us to propose a possible explanation for the seemingly fast second sound observed in many triangulation experiments. The formation of the cavitation zone is a very fast process, considering the rapid growth of the vapor bubbles as estimated in the previous section. The second-sound waves are indeed emitted from the surface of the cavitation zone instead of the heater surface. Therefore, for a second-sound sensor placed at a distance S from the heater surface, the actual distance traveled by the second sound is $S' = S - r_c$, where r_c denotes the size of the cavitation zone and is typically much smaller than S. As a consequence, the shorter travel time of the second-sound waves leads to a higher measured speed as given by $c_2' \simeq c_2(1 + r_c/S)$. This simple idea is supported by the experimental observation that
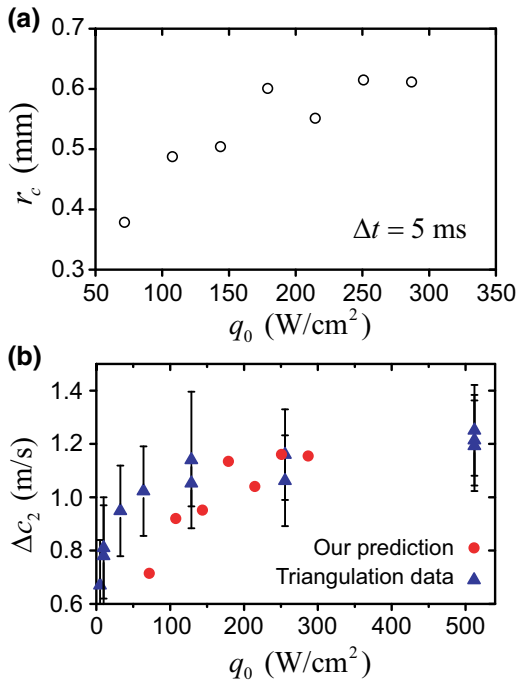
FIG. 8.   (a) Estimated radius r_c of the cavitation zone in our experiment as a function of the heat flux q_0. (b) Our predicted excess second-sound velocity Δc_2 in comparison with the triangulation data extracted from Refs. [22,65].

the fast second sound can be observed only in quench-spot experiments with high heat fluxes such that film boiling (i.e., cavitation) does occur near the hot spot [22,64].

To evaluate the excess velocity $\Delta c_2 = c_2' - c_2$, let us first estimate r_c. If we assume that the cavitation zone has a hemispherical surface with a radius r_c and that the heat flux on this surface is about the threshold for film boiling (i.e., 15 W/cm^2 [48]), r_c can be estimated based on

$$\frac{\dot{Q}_s}{2\pi r_c^2} = \frac{Q_s/\Delta t}{2\pi r_c^2} = 15 \text{ W/cm}^2. \qquad (8)$$

The calculated r_c values for our experiment are listed in Table I. r_c appears to be nearly independent of the pulse duration Δt but increases with increasing the heat flux q_0 from the heater surface as shown in Fig. 8(a). Since $\Delta c_2 = (c_2/S)r_c$, this result agrees with the trend observed in previous triangulation experiments that the measured second-sound speed increases with increasing the heat flux [21,22]. More interestingly, since r_c^2 scales with $\dot{Q}_s$ (and hence $\dot{Q}_0$) according to Eq. (8), for a given heat flux q_0, r_c^2 then scales with the heater area A_h. If we consider the triangulation results reported in Refs. [22,65] and scale r_c^2 based on their heater size $A_h = 15$ mm^2, we can indeed compute the excess velocity Δc_2 for their OST sensor placed at $S = 5$ cm from their heater surface. The results are shown in Fig. 8(b). The blue triangles are triangulation data extracted from Fig. 5 in Ref. [65]. Amazingly, our

predicted Δc_2 agrees quantitatively with the triangulation experimental observations. We must note that in reality the cavitation zone does not take a perfect hemispherical shape, especially when the heater size is large and the heat flux is small. This is probably why the triangulation data in Fig. 8(b) show relatively large difference from our predictions at small heat fluxes. Nevertheless, the overall excellent agreement between our model prediction and the triangulation observations provides strong support for the validity of our model.

C. 3D quench-spot detection for real SRF cavities

In the proof-of-concept experiment presented in Sec. II, we create the He$_2^*$ tracer lines in the vertical plane above a chosen miniature heater. The deformation of the tracer line only provides us the position information of the heater along the line where the vertical plane intersects with the PCB. In order for quench-spot detection on the 2D surface of a real SRF cavity, our technique needs to be advanced. For instance, a simple extension of the current method could be to create two orthogonal tracer lines near the surface. The deformations of the two lines will then provide us complimentary information about the hot-spot location along two orthogonal directions. A more preferable and accurate detection scheme that we would like to propose is shown in Fig. 9.

Instead of creating two tracer lines, we may first shape the fs-laser beam into a laser sheet and then pass it through a screen with parallel thin open slots to create an array of tracer lines. This can be done since the maximum pulse energy of our femtosecond laser (i.e., 4 mJ) is far greater than necessary for the creation of a single tracer line (i.e., 60 μJ [30]). Overlapping two such tracer-line arrays can
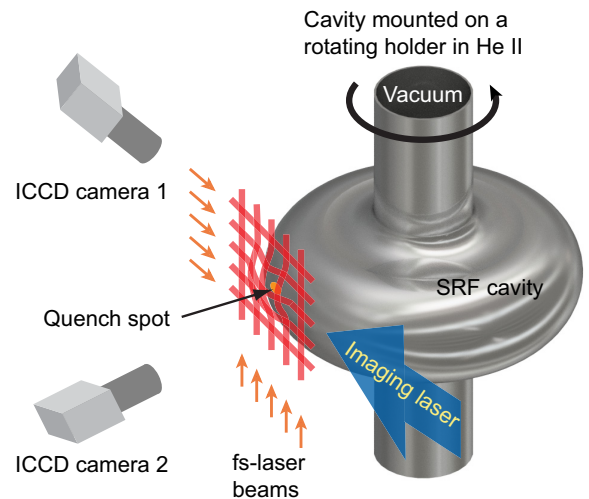

FIG. 9.   Schematic diagram showing the 3D quench-spot detection scheme for real SRF cavities using a tracer-line grid.

form a tracer-line grid, which has already been demonstrated in molecular tagging experiments in water [66]. We may create such a tracer-line grid near a cavity surface and implement 3D imaging using two ICCD cameras placed at different angles [67]. Once a quench event is detected through monitoring the dissipation of the rf field in the cavity [11], we can send in the imaging laser pulses to visualize the tracer-line grid. Due to the heat transfer from the quench spot to He II, a local deformation of the grid is expected. The analysis of this deformation will likely involve more fitting parameters. For instance, we may assume a Gaussian temperature profile in the hot area on the outer surface of the cavity. Then, besides the center position of the hot area and the transported heat in He II, other parameters such as the width of the Gaussian profile and the curvature radius of the surface may also be needed in the convolution of the initial grid profile to its final deformed profile. Finally, a scanning procedure may be implemented. By mounting the cavity on a rotating holder, we may use the same tracer-line grid to scan across the entire surface of the cavity so as to identify all surface defects.

V. SUMMARY

We have conducted a proof-of-concept experiment to demonstrate the feasibility of a flow-visualization-based noncontacting technology for SRF cavity quench-spot detection. By examining the deformation of a thin He_2^* molecular tracer line created in He II nearby a miniature heater following a short heat pulse, we are able to reconstruct the heater location within a few hundred microns. The actual heat transported through He II by the propagating second-sound zone is found to be only a small fraction of the total injected heat energy. Our analysis shows that the remaining heat energy is essentially consumed in the formation of a cavitation zone surrounding the heater. The size of this cavitation zone is estimated based on the knowledge obtained about the transported heat. This information has allowed us to propose an alternative explanation for the decades-long puzzle observed in previous second-sound triangulation experiments regarding heat transfer at speeds higher than literature values. The excellent quantitative agreement between our predicted excess second-sound velocity and those measured in triangulation experiments provides strong support for our model.

ACKNOWLEDGMENTS

[1] A. Nassiri, B. Chase, P. Craievich, A. Fabris, H. Frischholz, J. Jacob, E. Jensen, M. Jensen, R. Kustom, and R. Pasquinelli, History and technology developments of radio frequency (RF) systems for particle accelerators, IEEE Trans. Nucl. Sci. **63,** 707 (2016).

[2] H. Padamsee, 50 years of success for SRF accelerators—a review, Supercond. Sci. Technol. **30,** 053003 (2017).

[3] H. Padamsee, J. Knobloch, and T. Hays, *RF Superconductivity for Accelerators*, Wiley Series in Beam Physics and Accelerator Technology (Wiley, New York, 2008).

[4] M. Ge, G. Wu, J. Ruan, J. Ozelis, E. Borissov, T. Nicol, D. Hicks, D. A. Sergatskov, and L. D. Cooley, in *Proceedings of SRF2011* (Chicago, 2011), p. 740.

[5] K. Watanabe, H. Hayano, and Y. Iwashita, in *Proceedings of SRF2011* (Chicago, 2011), p. 598.

[6] Z. A. Conway, M. Ge, and Y. Iwashita, Instrumentation for localized superconducting cavity diagnostics, Supercond. Sci. Technol. **30,** 034002 (2017).

[7] J. Knobloch, H. Muller, and H. Padamsee, Design of a high speed, high resolution thermometry system for 1.5 GHz superconducting radio frequency cavities, Rev. Sci. Instrum. **65,** 3521 (1994).

[8] A. Canabal, T. Tajima, F. Krawczyk, W. Haynes, R. Roybal, J. Sedillo, and S. Cohen, in *Proceedings of EPAC08* (Genoa, 2008), p. 841.

[9] Q. S. Shu, T. Junquera, A. Caruette, G. Deppe, M. Fouaidy, W.-D. Moeller, M. Pekeler, D. Proch, D. Renken, and C. Stolzenburg, in *Advances in Cryogenic Engineering, A Cryogenic Engineering Conference Publication* (Springer, Boston, 1996), p. 895.

[10] H. Sakai, K. Shinoe, T. Furuya, T. Takahashi, T. Umemori, and M. Sawamura, in *Proceedings of EPAC08* (Genoa, 2008), p. 907.

[11] Z. A. Conway, D. L. Hartill, H. S. Padamsee, and E. N. Smith, in *Proceedings of SRF2009* (Berlin, 2009), p. 113.

[12] D. R. Tilley and J. Tilley, *Superfluidity and Superconductivity* (Institute of Physics Publishing, Bristol and Philadelphia, 1990), 3rd ed.

[13] L. D. Landau and E. M. Lifshitz, *Fluid Mechanics* (Pergamon Press, Oxford, 1987), 2nd ed., Vol. 6.

[14] S. W. Van Sciver, *Helium Cryogenics*, International Cryogenics Monograph Series (Springer, New York, 2012), 2nd ed.

[15] R. A. Sherlock and D. O. Edwards, Oscillating superleak second sound transducers, Rev. Sci. Instrum. **41,** 1603 (1970).

[16] K. W. Shepard, C. H. Scheibelhut, P. Markovich, R. Benaroya, and L. M. Bollinger, Development and production of superconducting resonators for the argonne heavy ion linac, IEEE Trans. Magn. **15,** 666 (1979).

[17] A. Lunt, Z. Kovács, H. Furci, T. Koettig, F. Léaux, and G. Vandoni, Towards robust design of thin film transition edge sensors for use in the next-generation superconducting radio frequency cavities, Mater. Des. **122,** 403 (2017).

[18] Y. Maximenko, Can we locate the quench origin with second sound?, Fermilab PARTI 2010 Summer Internship Report Fermilab PARTI 2010 Summer Internship Report (Fermilab, USA, 2010).

[19] R. Eichhorn, D. Hartill, G. Hoffstaetter, and S. Markham, in *Proceedings of SRF2015* (Whistler, 2015), p. 804.

[20] R. Eichhorn and S. Markham, On the mystery of using helium's second sound for quench detection of a superconducting cavity, Phys. Procedia **67,** 822 (2015).

[21] B. J. Peters, Diploma Thesis, Karlsruhe Institute of Technology, Karlsruhe, 2014.

[22] T. Junginger, P. Horn, T. Koettig, K. Liao, A. Macpherson, and B. J. Peters, in *Proceedings of SRF2015* (Whistler, 2015), p. 201.

[23] J. Plouin, J. P. Charrier, C. Magne, L. Maurice, and J. Novo, in *Proceedings of SRF2013* (Paris, 2013), p. 739.

[24] M. Bertucci, A. Bosotti, L. Garolfi, P. Michelato, L. Monaco, D. Sertore, and C. Pagani, in *Proceedings of SRF2013* (Paris, 2013), p. 710.

[25] M. Wenskat, Automated optical inspection and image analysis of superconducting radio-frequency cavities, J. Instrum. **12,** P05016 (2017).

[26] Y. Iwashita, Y. Tajima, and H. Hayano, Development of high resolution camera for observations of superconducting cavities, Phys. Rev. Spec. Top. - Accel. Beams **11,** 093501 (2008).

[27] Y. Maximenko and D. A. Segatskov, *Quench dynamics in SRF cavities: Can we locate the quench origin with 2nd sound?*, FERMILAB-CONF-11-152-TD FERMILAB-CONF-11-152-TD (FERMILAB, United States, 2011).

[28] J. R. Torczynski, On the interaction of second sound shock waves and vorticity in superfluid helium, Phys. Fluids **27,** 2636 (1984).

[29] W. Guo, M. La Mantia, D. P. Lathrop, and S. W. Van Sciver, Visualization of two-fluid flows of superfluid helium-4, Proc. Natl. Acad. Sci. U. S. A. **111,** 4653 (2014).

[30] J. Gao, A. Marakov, W. Guo, B. T. Pawlowski, S. W. Van Sciver, G. G. Ihas, D. N. McKinsey, and W. F. Vinen, Producing and imaging a thin line of He_2^* molecular tracers in helium-4, Rev. Sci. Instrum. **86,** 093904 (2015).

[31] A. Marakov, J. Gao, W. Guo, S. W. Van Sciver, G. G. Ihas, D. N. McKinsey, and W. F. Vinen, Visualization of the normal-fluid turbulence in counterflowing superfluid ^{4}He, Phys. Rev. B **91,** 094503 (2015).

[32] A. Quadt, B. Schröder, M. Uhrmacher, J. Weingarten, B. Willenberg, and H. Vennekate, Response of an oscillating superleak transducer to a pointlike heat source, Phys. Rev. Spec. Top. - Accel. Beams **15,** 031001 (2012).

[33] M. Fouaidy, F. Dubois, J.-M. Dufour, D. Longuevergne, G. Michel, A. Maroni, and J.-F. Yaniche, in *Proceedings of SRF2013* (Paris, 2013), p. 714.

[34] M. Fouaidy, D. Longuevergne, F. Dubois, O. Pochon, and J.-F. Yaniche, Detection and location of SRF bulk niobium cavities quench using second sound sensitive sensors in superfluid helium, IOP Conf. Ser. Mater. Sci. Eng. **171,** 012110 (2017).

[35] A. V. Benderskii, R. Zadoyan, N. Schwentner, and V. A. Apkarian, Photodynamics in superfluid helium: Femtosecond laser-induced ionization, charge recombination, and preparation of molecular Rydberg states, J. Chem. Phys. **110,** 1542 (1999).

[36] A. V. Benderskii, J. Eloranta, R. Zadoyan, and V. A. Apkarian, A direct interrogation of superfluidity on molecular scales, J. Chem. Phys. **117,** 1201 (2002).

[37] D. N. McKinsey, C. R. Brome, J. S. Butterworth, S. N. Dzhosyuk, P. R. Huffman, C. E. H. Mattoni, J. M. Doyle, R. Golub, and K. Habicht, Radiative decay of the metastable $He_2(a^3\sum_u^+)$ molecule in liquid helium, Phys. Rev. A **59,** 200 (1999).

[38] W. G. Rellergert, S. B. Cahn, A. Garvan, J. C. Hanson, W. H. Lippincott, J. A. Nikkel, and D. N. McKinsey, Detection and Imaging of He_2 Molecules in Superfluid Helium, Phys. Rev. Lett. **100,** 025301 (2008).

[39] J. Gao, W. Guo, and W. F. Vinen, Determination of the effective kinematic viscosity for the decay of quasiclassical turbulence in superfluid ^{4}He, Phys. Rev. B **94,** 094502 (2016).

[40] J. Gao, W. Guo, V. S. L'vov, A. Pomyalov, L. Skrbek, E. Varga, and W. F. Vinen, Decay of counterflow in superfluid ^{4}He, JETP Lett. **103,** 648 (2016).

[41] J. Gao, E. Varga, W. Guo, and W. F. Vinen, Energy spectrum of thermal counterflow turbulence in superfluid helium-4, Phys. Rev. B **96,** 094511 (2017).

[42] J. Gao, W. Guo, S. Yui, M. Tsubota, and W. F. Vinen, Dissipation in quantum turbulence in superfluid ^{4}He above 1 K, Phys. Rev. B **97,** 184518 (2018).

[43] E. Varga, J. Gao, W. Guo, and L. Skrbek, Intermittency enhancement in quantum turbulence in superfluid ^{4}He, Phys. Rev. Fluids **3,** 094601 (2018).

[44] R. J. Donnelly and C. F. Barenghi, The observed properties of liquid helium at the saturated vapor pressure, J. Phys. Chem. Ref. Data **27,** 1217 (1998).

[45] W. F. Vinen, Mutual friction in a heat current in liquid helium II I. Experiments on steady heat currents, Proc. R. Soc. A **240,** 114 (1957).

[46] W. F. Vinen, Mutual friction in a heat current in liquid helium II III. Theory of the mutual friction, Proc. R. Soc. A **242,** 493 (1957).

[47] R. J. Donnelly, *Quantized Vortices in Helium II* (Cambridge University Press, Cambridge, 1991).

[48] T. Shimazaki, M. Murakami, and T. Iida, Second sound wave heat transfer, thermal boundary layer formation and boiling: Highly transient heat transport phenomena in He II, Cryogenics **35,** 645 (1995).

[49] T. Iida, M. Murakami, T. Shimazaki, and H. Nagai, Visualization study on the thermo-hydrodynamic phenomena induced by pulsative heating in He II by the use of a laser holographic interferometer, Cryogenics **36,** 943 (1996).

[50] D. K. Hilton and S. W. Van Sciver, Direct measurements of quantum turbulence induced by second sound shock pulses in helium II, J. Low Temp. Phys. **141,** 47 (2005).

[51] H. Schlichting, *Boundary-Layer Theory*. McGraw-Hill Series in Mechanical Engineering (McGraw-Hill, New York, 1979), 7th ed.

[52] S. Pulkkinen, M. M. Mäkelä, and N. Karmitsa, A generative model and a generalized trust region Newton method for noise reduction, Comput. Optim. Appl. **57,** 129 (2014).

[53] T. Zhang and S. W. Van Sciver, Use of the particle image velocimetry technique to study the propagation of second sound shock in superfluid helium, Phys. Fluids **16,** L99 (2004).

[54] W. F. Vinen, Mutual friction in a heat current in liquid helium II II. Experiments on transient effects, Proc. R. Soc. A **240**, 128 (1957).

[55] T. Shimazaki, M. Murakami, and T. Kanari, Measurement of characteristic time for quantized vortex tangle development in He II, Cryogenics **38**, 601 (1998).

[56] W. F. Vinen and J. J. Niemela, Quantum turbulence, J. Low Temp. Phys. **128**, 167 (2002).

[57] A. Prosperetti, Vapor bubbles, Annu. Rev. Fluid Mech. **49**, 221 (2017).

[58] M. K. Gupta, D. S. Sharma, and V. J. Lakhera, Vapor bubble formation, forces, and induced vibration: A review, Appl. Mech. Rev. **68**, 030801 (2016).

[59] W. Lauterborn and H. Bolle, Experimental investigations of cavitation-bubble collapse in the neighbourhood of a solid boundary, J. Fluid Mech. **72**, 391 (1975).

[60] A. Vogel, W. Lauterborn, and R. Timm, Optical and acoustic investigations of the dynamics of laser-produced cavitation bubbles near a solid boundary, J. Fluid Mech. **206**, 299 (1989).

[61] B. Liu, J. Cai, F. C. Li, and X. L. Huai, Simulation of heat transfer with the growth and collapse of a cavitation bubble near the heated wall, J. Therm. Sci. **22**, 352 (2013).

[62] P. Zhang, M. Murakami, and R. Z. Wang, Study of liquid column oscillation and vapour bubble oscillation resulting from film boiling in He II, J. Phys. Appl. Phys. **34**, 3296 (2001).

[63] E. S. Bosque, R. C. Dhuley, and S. W. Van Sciver, Transient heat transfer in helium II due to sudden vacuum break, AIP Conf. Proc. **1573**, 260 (2014).

[64] K. Liao, O. Brunner, E. Ciapala, T. Junginger, and W. Weingarten, in *International Particle Accelerator Conference* (N. Orleans, 2012).

[65] T. Koettig, B. J. Peters, S. Avellino, T. Junginger, and J. Bremer, Study of temperature wave propagation in superfluid helium focusing on radio-frequency cavity cooling, IOP Conf. Ser.: Mater. Sci. Eng. **101**, 012164 (2015).

[66] H. Hu and M. M. Koochesfahani, Molecular tagging velocimetry and thermometry and its application to the wake of a heated circular cylinder, Meas. Sci. Technol. **17**, 1269 (2006).

[67] D. G. Bohl, M. M. Koochesfahani, and B. J. Olson, Development of stereoscopic molecular tagging velocimetry, Exp. Fluids **30**, 302 (2001).